Wu, B.-W., Ma, J., **Banzhaf, E.**, Meadows, M.E., Yu, Z.-W., **Guo, F.**, Sengupta, D., Cai, X.-X., Zhao, B. (2023):
A first Chinese building height estimate at 10 m resolution (CNBH-10 m) using multi-source earth observations and machine learning
Remote Sens. Environ. **291** , art. 113578

https://doi.org/10.1016/j.rse.2023.113578

A first Chinese building height estimate at 10 m resolution (CNBH-10m) using multi-source earth observations and machine learning

Wan-Ben Wu[a,b], Jun Ma[a], Ellen Banzhaf[b], Michael E. Meadows[c,d], Zhao-Wu Yu[e], Feng-Xiang Guo[b,f], Dhritiraj Sengupta[g], Xing-Xing Cai[a], Bin Zhao[a*]

[a] Ministry of Education Key Laboratory for Biodiversity Science and Ecological Engineering, National Observations and Research Station for Wetland Ecosystems of the Yangtze Estuary, and Shanghai Institute of EcoChongming (SIEC), Fudan University, Shanghai, 200433, China (wbwu19@fudan.edu.cn; ma_jun@fudan.edu.cn; zhaobin@fudan.edu.cn; xxcai@fudan.edu.cn)

[b] Department of Urban and Environmental Sociology, UFZ – Helmholtz Centre for Environmental Research, Leipzig 04318, Germany (ellen.banzhaf@ufz.de; fengxiang.guo@ufz.de)

[c] School of Geographic and Ocean Sciences, Nanjing University, Nanjing, China

[d] Department of Environmental & Geographical Science, University of Cape Town, Cape Town 7701, South Africa (michael.meadows@uct.ac.za)

[e] Department of Environmental Science and Engineering, Fudan University, Shanghai 200433, China (zhaowuyu@fudan.edu.cn)

[f] Faculty of Physics and Earth Sciences, Leipzig University, Leipzig 04109, Germany (fengxiang.guo@uni-leipzig.de)

[g] School of Geography and Environmental Science, University of Southampton, Southampton SO17, UK (d.sengupta@soton.ac.uk)

Highlights:

- The first country-wide 10 m building height map for China
- Shading index is the most important variable in estimating building height
- High degree of building height accuracy with RMSE of 6.1 m

Abstract

Building height is a crucial variable in the study of urban environments, regional climates, and human-environment interactions. However, high-resolution data on building height, especially at the national scale, are limited. Fortunately, high spatial-temporal resolution earth observations, harnessed using a cloud-based platform, offer an opportunity to fill this gap. We describe an approach to estimate 2020 building height for China at 10 m spatial resolution based on all-weather earth observations (radar, optical, and night light images) using the Random Forest (RF) model. Results show that our building height simulation has a strong correlation with real observations at the national scale (RMSE of 6.1 m, MAE=5.2 m, R=0.77). The Combinational Shadow Index (CSI) is the most important contributor (15.1%) to building height simulation. Analysis of the distribution of building morphology reveals significant differences in building volume and average building height at the city scale across China. Macau has the tallest buildings (22.3 m) among Chinese cities, while Shanghai has the largest building volume (298.4 10^8 m^3). The strong correlation between modelled building volume and socio-economic parameters indicates the potential application of building height products. The building height map developed in this study with a resolution of 10 m is open access, provides insights into the 3D morphological characteristics of cities and serves as an important contribution to future urban studies in China.

Keywords: Multi-Sensor; Machine learning; Urban morphology; Google Earth Engine; Building height

1. Introduction

Accurate measurement of building height is essential for understanding the impacts of urbanization on the urban environment. Building height is correlated with urban energy use (Resch et al. 2016), greenhouse gas emissions (Borck 2016; Marconcini et al. 2020) and human wellbeing (Liang et al. 2020; Schug et al. 2021). Furthermore, it is a crucial variable in volumetric analysis (Sun et al. 2018), population mapping (Alahmadi et al. 2013) and living conditions such as *per capita* space availability (Ghosh et al. 2020). Building height also has a significant impact on urban climate (Xi et al. 2021), including urban heat islands effects (Huang and Wang 2019; Perini and Magliocco 2014; Wu et al. 2022), solar radiation (Cheng et al. 2020; Sorichetta et al. 2015) and wind speeds (Miao et al., 2009). Accurate mapping of building height is therefore an important basis in improving our understanding of urban processes.

In recent decades, two-dimensional (2D) urban morphology, including urban boundaries, the extent of impervious surface, and human settlement footprints, have received considerable attention and resulted in many high-resolution and global products (Gong et al. 2020; Li et al. 2020b; Marconcini et al. 2020; Mertes et al. 2015). There are, however, relatively few studies or products available for three-dimensional (3D) urban structures, and most of these focus on particular cities with spatial resolution limited to 0.3-1km (Kedron et al. 2019; Li et al. 2020c; Yang and Zhao 2022; Zhang et al. 2018). Even scarcer are 3D high-resolution data for urban structures in large and connected areas (Zhu et al. 2019).

Currently, open-source and freely available earth observations are widely used for 3D mapping of urban morphology. For example, using Sentinel-1 backscatter data, Li et al. (2020c) modelled building height at 500 m spatial resolution for major cities in the US. Yang and Zhao (2022) presented a building height map for China at 1km-spatial-resolution based on Sentinel-1 data and spatially-informed Gaussian process regression. However, the accuracy and application of such models is constrained by the backward scattering coefficient which is influenced not only by building height but also by the surface characteristics of construction materials, the composition of land-cover surrounding the buildings, and by the roughness characteristics of buildings or trees (Koppel et al. 2017; Vreugdenhil et al. 2018). It is possible to address these limitations, Huang et al. (2022), developed a method to estimate building height for China based on the Advanced Land Observing Satellite (ALOS) World 3D-30 m (AW3D30) DSM (Huang et al. 2022). As illustrated by Frantz et al. (2021), who combined Sentinel-1A/B and Sentinel-2A/B time series data to construct a model of building height for the whole of Germany. However, China has a more complex urban 3D structure, greater degree of building heterogeneity, and a wider distribution of high-rise buildings (Li et al. 2020a) and accordingly the method requires further modification to produce a reliable estimate building height at the national scale.

An accurate map of building height is a basic requirement to support urban environmental research and planning, the more so in China with its prolific and rapid scale of urbanization. To date, however, there is no high resolution (less than 30 m) map of building height on a national scale. In filling this research gap, this study aims to develop a first Chinese building height map at 10 m resolution (CNBH-10 m) based on data from an open-source earth observation platform analysed using machine learning. The main research objectives of the study are as follows:

(1) To construct high-resolution building height estimation models using data from multiple-source, multi-temporal, and multi-scale to accommodate complex urban structures at the national scale in China.

(2) To evaluate the accuracy and generalizability of building height models in different regions of the country.

(3) To explore the distribution of different building forms in China and the factors underlying this distribution.

2. Data Description

2.1 Independent variables

As summarized in Table 1, the independent variables used to estimate building height include radar data, optical data, night-time light data, population data, topographic data, and settlement distribution data. Each variable and preprocessing step is described in detail below. We did not filter the variables for further regression because the RF model is insensitive to multivariate linearity (Breiman 2001).

2.1.1 Sentinel-1

Sentinel-1 Ground Range Detected (GRD) scenes were used to estimate urban building height which provides data from a dual-polarization C-band Synthetic Aperture Radar (SAR) instrument. Sentinel-1 imageries are available at 10 m resolution and a short revisit time (6-12 days) (Dai et al. 2016). In this study, two polarization bands, VV and VH, and dual-polarization information derived VVH (Li et al. 2020c) were used for further building height estimation. All Sentinel-1 SAR GRD data are available on the GEE platform (Gorelick et al. 2017), and all the data on GEE were processed using Sentinel-1 Toolbox (Veci et al. 2014) to generate a calibrated, ortho-corrected product. A total of 56,821 scenes of Sentinel-1 data were used in this study. Fig. 1a shows the total observations of Sentinel-1 data from 2019 to 2021.

The dual-polarised information derived VVH was calculated as follows:

$$VVH = \mathrm{VV} * \gamma^{VH} \quad (1.)$$

Where γ was set to 5 based on a former study (Li et al. 2020c).

2.1.2 PALSAR

Phased Array Type L-band Synthetic Aperture Radar (PALSAR) is an active microwave sensor which has a multi-polarization configuration, and is widely used for the estimation of vertical structure in vegetation. In this study, global 25 m PALSAR/

PALSAR-2 yearly mosaic data from 2019 to 2021 were obtained from the GEE data catalog (Collection Snippet: "JAXA/ALOS/PALSAR/YEARLY/SAR"). To ensure high-quality data, the SAR images with the lowest response to surface moisture were prefer used for creating the annual product using the mean composite method (Shimada et al. 2014).

2.1.3 Sentinel-2

In this study, a total of 160,023 scenes of Sentinel-2 were utilized. The QA60 bitmask band was used to mask out poor-quality observations caused by clouds (Bit 10) and cirrus clouds (Bit 11) (Ni et al. 2021) for each image. Fig. 1b shows the total number of cloud free observations of Sentinel-2 data during 2019 to 2021. In addition to Sentinel-2 bands, six other spectral indices were considered as independent variables, including Normalized Difference Vegetation Index (NDVI) (Pettorelli 2013; Tucker 1979), Enhanced Vegetation Index (EVI) (Huete et al. 2002), Land Surface Water Index (LSWI) (Xiao et al. 2004), Modified Normalized Difference Water Index (MNDWI) (Xu 2006), Normalized Difference Built-up Index (NDBI) (Zha et al. 2003), and Combinational Shadow Index (CSI) (Sun et al. 2019). Equations used to calculate the indices are as follows:

$$NDVI = \frac{\rho_{NIR} - \rho_{red}}{\rho_{NIR} + \rho_{red}} \qquad (2.)$$

$$EVI = \frac{2.5(\rho_{NIR} - \rho_{red})}{(\rho_{NIR} + 6\rho_{red} - 7.5\rho_{blue} + 1)} \qquad (3.)$$

$$LSWI = \frac{\rho_{NIR} - \rho_{swir1}}{\rho_{NIR} + \rho_{swir1}} \qquad (4.)$$

$$MNDWI = \frac{\rho_{green} - \rho_{swir1}}{\rho_{green} + \rho_{swir1}} \qquad (5.)$$

$$NDBI = \frac{\rho_{swir1} - \rho_{NIR}}{\rho_{swir1} + \rho_{NIR}} \qquad (6.)$$

$$SEI = \frac{(\rho_{aerosols} + \rho_{water\ vapor}) - (\rho_{green} + \rho_{NIR})}{(\rho_{aerosols} + \rho_{water\ vapor}) + (\rho_{green} + \rho_{NIR})} \qquad (7.)$$

$$CSI = \begin{cases} SEI - \rho_{NIR}, if\ \rho_{NIR} \geq NDWI \\ SEI - NDWI, else \end{cases} \quad (8.)$$

where ρ_{red}, ρ_{green}, ρ_{blue}, ρ_{NIR}, ρ_{swir1}, $\rho_{aerosols}$, $\rho_{water\ vapor}$ are the surface reflectance of the red, green, blue, near infrared, shortwave infrared, aerosols and water vapor bands of the Sentinel-2 MSI sensor.

2.1.4 LUOJIA night light image

LUOJIA 1-01, a new nighttime light (NTL) data satellite launched by China in 2018, has a spatial resolution of 130 meters (Li et al. 2018). In this investigation, we utilized LUOJIA night light images from 2018 as input data to derive estimations of building heights. To improve the accuracy of NTL, we calculated the Vegetation Adjusted NTL Urban Index (VANUI) (Zhang et al. 2013) based on *equation 9* to mitigate the oversaturation effect of NTL.

$$VANUI = (1 - \mathrm{NDVI}) * \mathrm{NTL} \quad (9.)$$

where NDVI is the annual mean NDVI derived from Landsat products in 2018 and NTL is the DN value of LUOJIA 1-01 NTL data.

2.1.5 Settlement footprint

The World Settlement Footprint (WSF) layer for 2019 is a global human settlement distribution product at a ground resolution of 10 m derived from Landsat-8 and Sentinel-1 data. In this study, the settlement coverage derived from WSF 2019 was extracted as an independent variable for building height estimation and was also used to mask the final CNBH-10m product to remove to remove non-built-up pixels. We chose WSF due to its superior ability to remove roads between buildings, as well as its high user accuracy and accuracy of area estimation compared to other datasets such as ESA WorldCover, ESRI Land Cover, and GHS-BUILT-S2 (Wang et al. 2022). Fig. 1c shows the distribution of WSF in 2019.

2.1.6 Other independent variables

Considering the large extent of mainland China's latitude and longitude range, from 73°33′E to 135°05′E and from 3°51′N to 53°33′N, we incorporated the potential impact of variations in solar elevation angle on the model in our selection of variables for building height inversion. We included building location (longitude and latitude) and topographic information (DEM and slope) as key variables, as these factors significantly affect the solar elevation angle. In addition, population size was considered as an independent variable. More detailed information on the data sets used here is presented in Table 1. All variables were resampled to 10 m using the nearest neighbor resampling method for building height modeling and estimation.

2.2 Reference building height dataset

The vector building footprint data, which incorporate the information relating to the number of floors for 62 cities in China for the year 2018 (Fig. 1d) were collected from Baidu map services (http://www.map.baidu.com). To obtain the building height for each building, the number of building floors was multiplied by 3 m (Tripathy et al. 2022; Wu et al. 2022). Liu et al. (2021) report an accuracy of 86.8%, with a mean height deviation of approx. 1 m, for this dataset. In order to acquire sample points of building footprint for further analysis, we used the method (equation 10) from Frantz et al. (2021) to convert the vector building height data of single buildings to 10 m spatial resolution grid data. In order to enhance the quality of samples and mitigate errors arising from incomplete building measurements, the analysis excluded samples within a 50-meter radius of the sampling point that exhibited a difference of more than 25% between the building footprint vector data and the WSF building distribution in terms of area. In this study, a total of 22,909 samples were used to train (70%) and validate (30%) the building height model.

$$BH_{10m} = \frac{\sum_p^n H_p * A_p}{\sum_p^n A_p}$$

(10.)

where H_p and A_p represent the height and area of individual building patches, respectively, while $\sum_p^n A_p$ denotes the total area of all building patches within the statistical area.

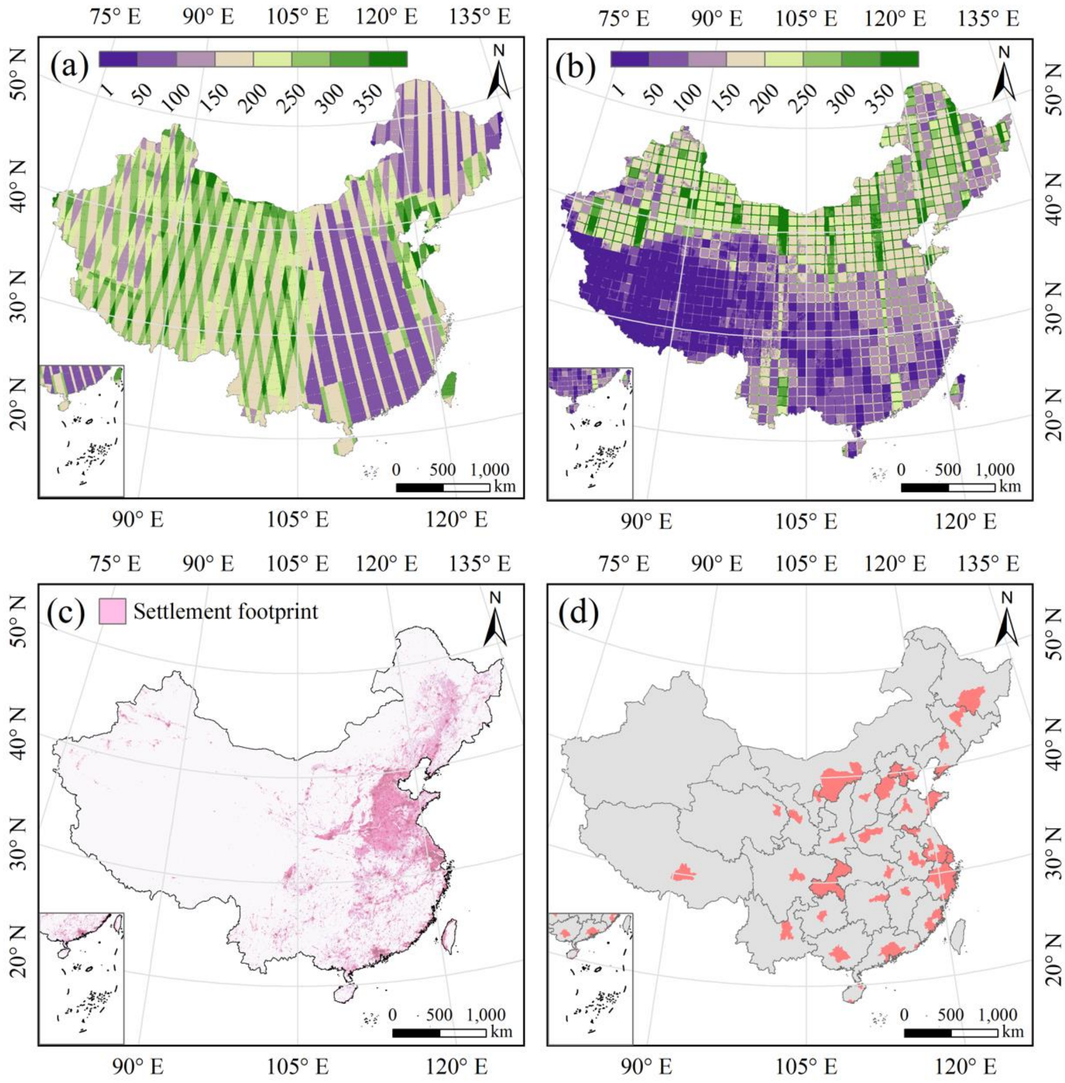

Fig. 1 Study area and data availability. (a) number of Sentinel-1 observations from 2019 to 2021; (b) number of cloud free Sentinel-2 observations from 2019 to 2021; (c) human settlement footprint of China in 2019; (d) reference building height data distribution (colored polygon).

Table 1. Datasets used to estimate building height

Code	Products	Variables	Acquisition time	Resolution	Data Source	Reference
0	Reference building height	building height	2019	Vector	http://www.map.baidu.com	(Liu et al. 2021)
1-3	Sentinel-1	VV; VH; VVH	2019-2021	10 m	"COPERNICUS/S1_GRD" (Collection Snippet in GEE)	(Torres et al. 2012)
4-5	PALSAR	HH; HV	2019-2021	25 m	"JAXA/ALOS/PALSAR/YEARLY/SAR" (Collection Snippet in GEE)	(Shimada et al. 2014)
6-22	Sentinel-2	Aerosols; Blue; Green; Red; NIR; Red Edge 1-4; SWIR 1; SWIR 2; NDVI; EVI; LSWI; MNDWI; NDBI; CSI	2019-2021	10/20/60 m	"COPERNICUS/S2_SR" (Collection Snippet in GEE)	(Drusch et al. 2012)
23	LUOJIA 1-01	VANUI	2018	130 m	http://www.hbeos.org.cn	(Li et al. 2018)
24	World population	Population	2020	100 m	"WorldPop/GP/100 m/pop" (Collection Snippet in GEE)	(Sorichetta et al. 2015)
25-26	SRTM	DEM; Slope	2000	90 m	https://srtm.csi.cgiar.org	(Rodriguez et al. 2006)
27	WSF 2019	Settlement coverage	2019	10 m	https://geoservice.dlr.de/web/maps/eoc:wsf2019	(Marconcini et al. 2020)
28-29	Location	Latitude; Longitude	/	10 m	/	/

3. Methodology

Fig. 2 illustrates the workflow developed for the building height estimation based on multi-source, multi-temporal, all-weather earth observations. The approach consists of three main sections. First, the preprocessing of independent variables was conducted by combining multi-temporal, multi-spectral, multi-window, and multi-statistical methods. Second, the Random Forest (RF) model was used to construct and optimize the estimation model. Third, the validation of the simulations was referenced against real building height data.

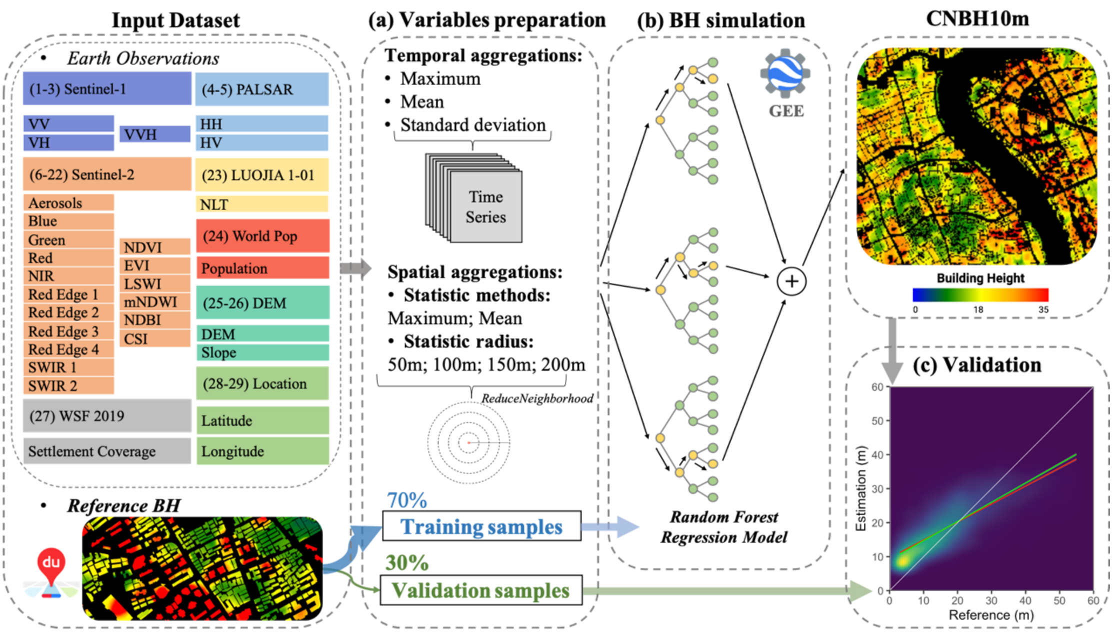

Fig. 2 Method overview of CNBH-10 m estimation

3.1 Preparation of variables

All Sentinel-1 and cloud free Sentinel-2 time series were temporally aggregated to enhance the richness of information. This processing step employed the spectral-temporal variability approach (Frantz et al. 2021). We calculated the maximum, minimum, and standard deviation of the time series of Sentinel-1, Sentinel-2, and their derivatives variables for the three-year period from 2019 to 2021. To capture shadow features across different levels of building heights, we employed multi-window local statistics (Figure 3) that utilized both spectral features and radar data. We applied maximum and mean statistical methods to circles with radii of 50 m, 100 m, 150 m, and 200 m.

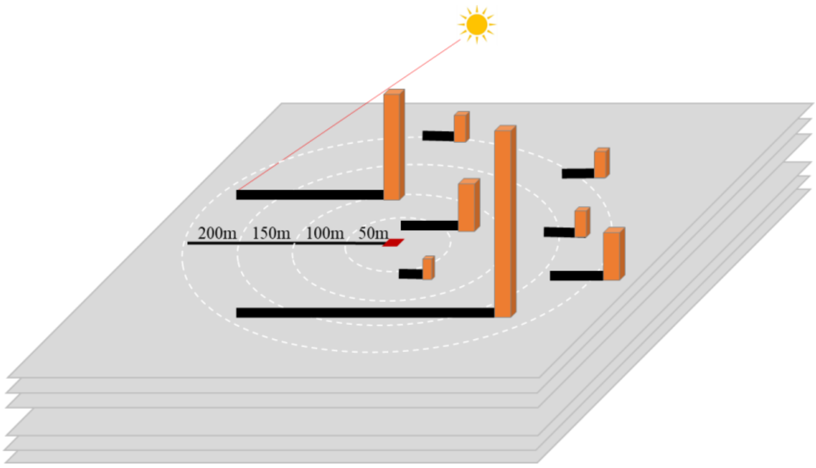

Fig. 3 Method of multi-window statistics

3.2 Building height model

The RF regression model (Liaw and Wiener 2002) was used to estimate building height, where a total of 519 variables were set as predictors, and 22,909 samples were used as training samples. The number of trees (Ntree) and the number of features randomly selected to split each node (Mtry) are two crucial parameters of the RF model. Increasing Ntree can enhance the performance of random forests. Since the RF classifier is computationally efficient and non-overfitting, Ntree can be set to the highest feasible value (Guan et al. 2013). In most of the studies reviewed here, the Ntree value was set at 500, as the errors of the classification tree stabilize before this number is reached (Lawrence et al. 2006). When Mtry is small, the model's variance decreases, but the bias increases, as some critical features may be ignored. When Mtry is large, the variance of the model increases, but the bias decreases as the model considers more features. Previous research suggests using the square root of the number of variables as the value for Mtry (Gislason et al. 2006). Therefore, in this study, we set Ntree and Mtry to 600 and the square root of the number of variables, respectively. In order to understand the importance of different variables for the building height model, the relative importance of each variable was evaluated using the Mean Decrease in Gini

(MDG) method (Breiman 2001). For 2019, WSF data were used to define the settlement footprint of the CNBH-10 m map. The RF regression model was performed on the Google Earth Engine (GEE) platform (Gorelick et al. 2017).

3.3 Accuracy assessment

To assess the accuracy of the estimated building height, three indicators were calculated including R, Root Mean Square error (RMSE) and Mean Absolute Error (MAE) based on 30% of the reference samples. In this study, we evaluated the accuracy of the model using both the least squares (LS) regression model and the weighted least squares (WLS) regression model. The WLS model assigns weights to each building height category, with data points appearing more frequently in the height category having a lower weight, resulting in a more precise estimation of the slope of the regression line.

$$R = \sqrt{1 - \frac{(n-1)\sum_{i=1}^{n}(BH_{est,i} - BH_{ref,i})^2}{(n-2)\sum_{i=1}^{n}(BH_{est,i} - BH_{ref,i})^2}} \tag{11.}$$

$$RMSE = \sqrt{\frac{\sum_{i=1}^{n}(BH_{est,i} - BH_{ref,i})^2}{n}} \tag{12.}$$

$$MAE = \frac{\sum_{i=1}^{n}\left|BH_{est,i} - BH_{ref,i}\right|}{\mathrm{n}} \tag{13.}$$

where n is the number of validation samples, $BH_{est,i}$ is the estimated building height value, and $BH_{ref,i}$ is the reference building height value.

4. Results

4.1 Relative importance of variables

Fig. 4 illustrates the relative importance of each independent variable in the building height estimation model. The cumulative relative importance (Fig. 4 a) indicates that the CSI makes the largest contribution (15.1%) to the estimation model, followed by VH (7.8%). Overall, the contribution of optical, radar, and other data to the building height estimation model is 76.6%, 18.2%, and 5.3%, respectively.

According to the average degree of importance of each independent variable (Fig. 4 b), building location (latitude, longitude, DEM, slope), and settlement density also contribute to the simulation, albeit less so. The importance of information gathered by windows of different sizes varies for building height models, as the relative importance of the 50 m, 100 m, 150 m, and 200 m scales are 34.2%, 32.5%, 22.4%, and 5.6%, respectively. To summarize, optical information exhibits the highest level of importance in combination with the most significant scales of 50 and 100 m.

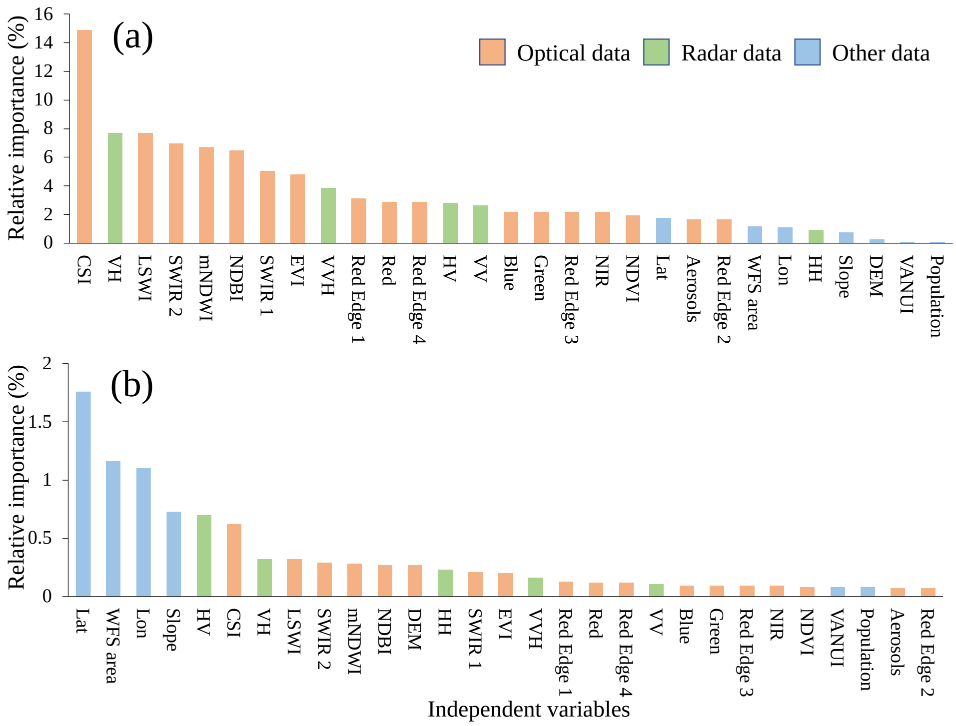

Fig. 4. (a) Cumulative and (b) average relative importance of each variable under various spatial-temporal fusion methods

The results in Figure 5 show the progression of estimation accuracy as the number of variables increases. A total of 519 models were constructed by incrementally adding variables based on their relative importance, and the change in model accuracy was assessed as the number of independent variables increased. The results indicate that the inclusion of a certain number of variables significantly improves estimation accuracy, but that further increasing the number of variables eventually reaches a plateau at which accuracy can no longer be improved. Therefore, a balance between efficiency and high estimation accuracy can be achieved by including a specific number (121 in this study) of variables in the model.

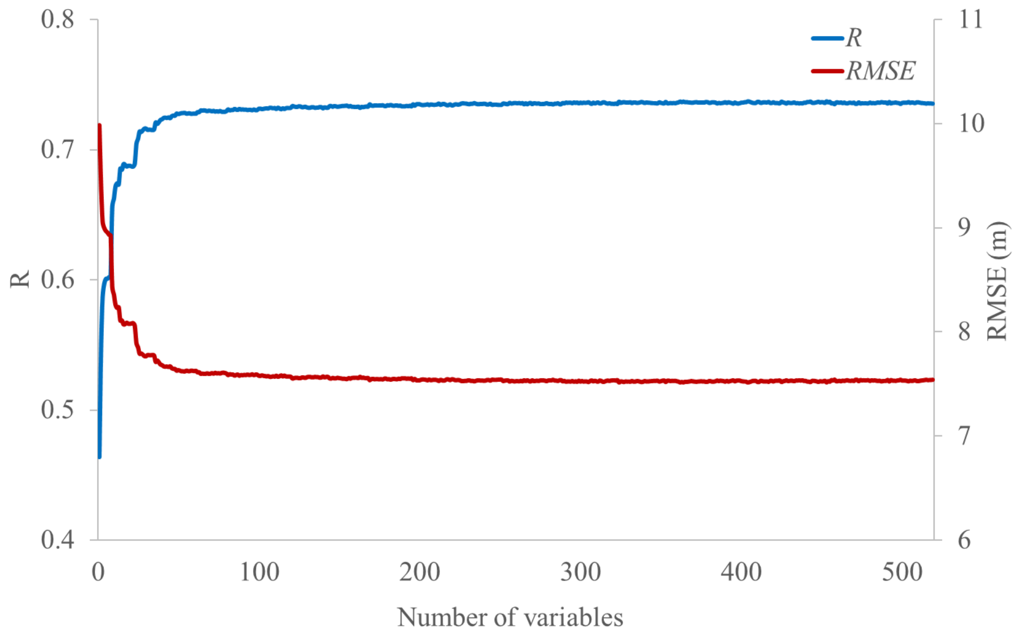

Fig. 5. The relationship between the number of input variables and the R (blue line) and RMSE (red line) values of the estimation models.

4.2 Accuracy assessment

Figure 6 illustrates the relationship between reference and estimated building height. Our study confirms the remarkable generalizability of the RF-based building height model across various cities. Using the least squares regression model, the mean values of R, RMSE, and MAE were 0.7, 7.6 m, and 6 m, respectively. Meanwhile, the WLS regression models produced mean values of R, RMSE, and MAE at 0.7, 6.2 m, and 5.2 m, respectively. The three strongest correlations based on WLS regression models are obtained for the dataset in Nantong (R=0.87), Beijing (R=0.82) and Tangshan (R=0.8). Wuhu (4.1 m), Baoding (4.2 m), and Quanzhou (4.5 m) exhibit the smallest RMSE. The validation results for all samples exhibit a strong statistical relationship between the estimated and reference building heights (R=0.77 using both least squares regression and WLS regression models). In the least squares regression model, the model achieved an uncertainty (RMSE) of 7.4 m and MAE of 5.8 m, in the WLS regression model the RMSE was 6.1 m and MAE was 5.2 m. Figure 7 shows the distribution of accuracy obtained from two evaluation models. Further results of the accuracy verification for individual cities can be found in the supplementary Figure S1 and Table S1.

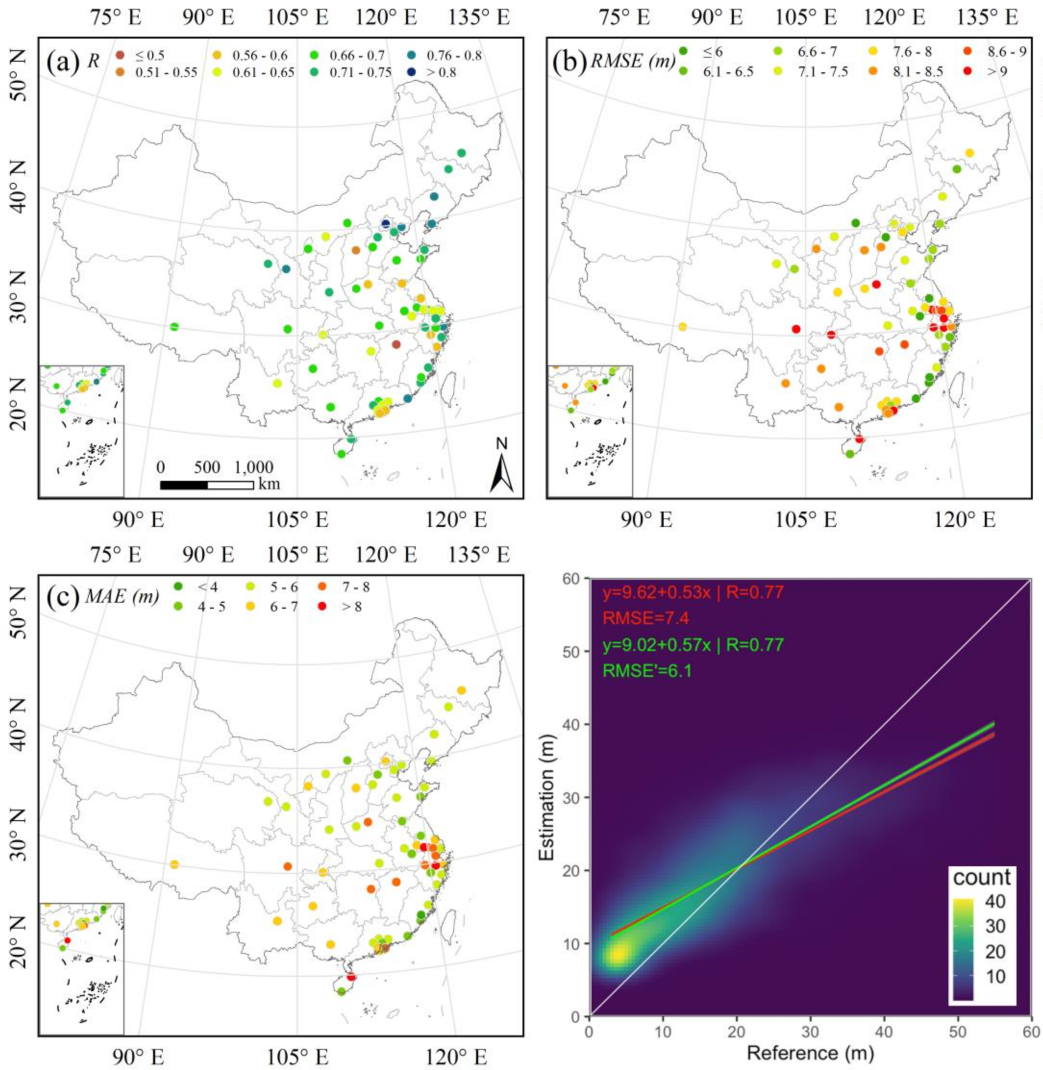

Fig. 6. Building height validation based on building footprint data, (a) R, (b) RMSE, (c) MAE distribution for each city, and (d) validation results based on all the samples, white line: one-to-one, red line: ordinary least squares regression, green line: WLS regression, text in red: regression model, R value and RMSE of the ordinary least squares model, text in green: regression model, R value and RMSE of the WLS regression model.

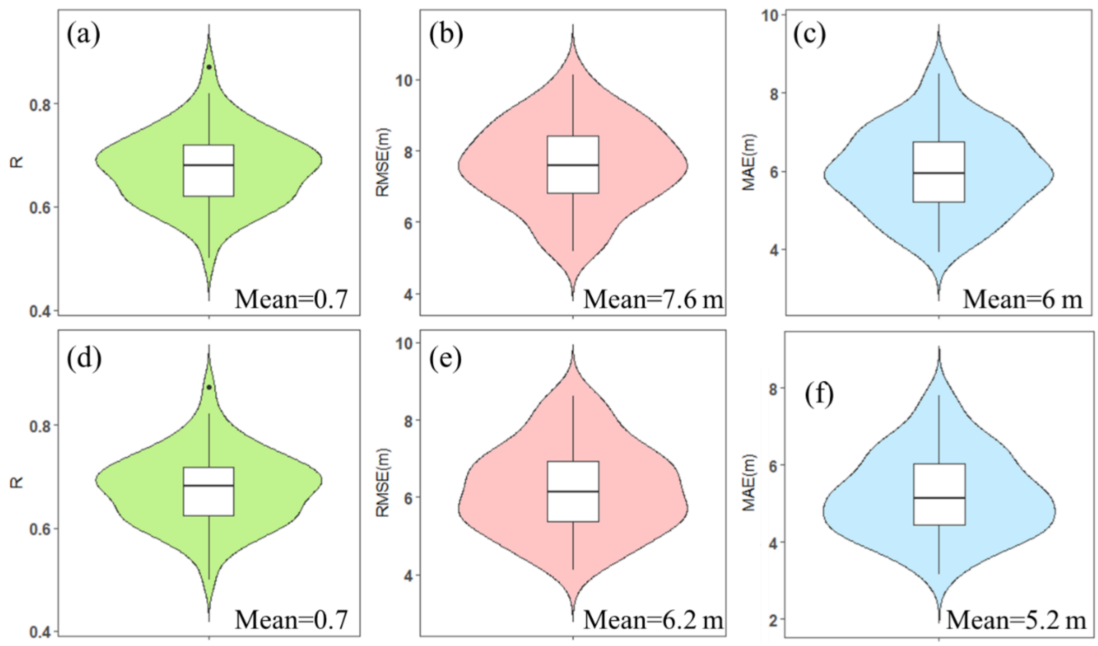

Fig. 7. The violin plots illustrate the distribution of estimation accuracy for building heights based on validation samples from 62 cities. (a)-(c) represent the results of evaluation based on LS regression models, while (d)-(f) represent the results of evaluation based on WLS regression models. The boxplots inside each violin show the median, quartiles, and range of estimation accuracy.

4.3 Spatial patterns of building height

Figure 8 indicates the height distribution of buildings in China in 2020. The results reveal that megacities in eastern China. More specifically in the Yangtze River Basin and Delta, the Beijing-Tianjin-Hebei region and Guangzhou-Shenzhen-Hong Kong regions have the greatest concentrations of high-rise buildings. As would be expected, large and medium-sized urban centers also have signify taller buildings.

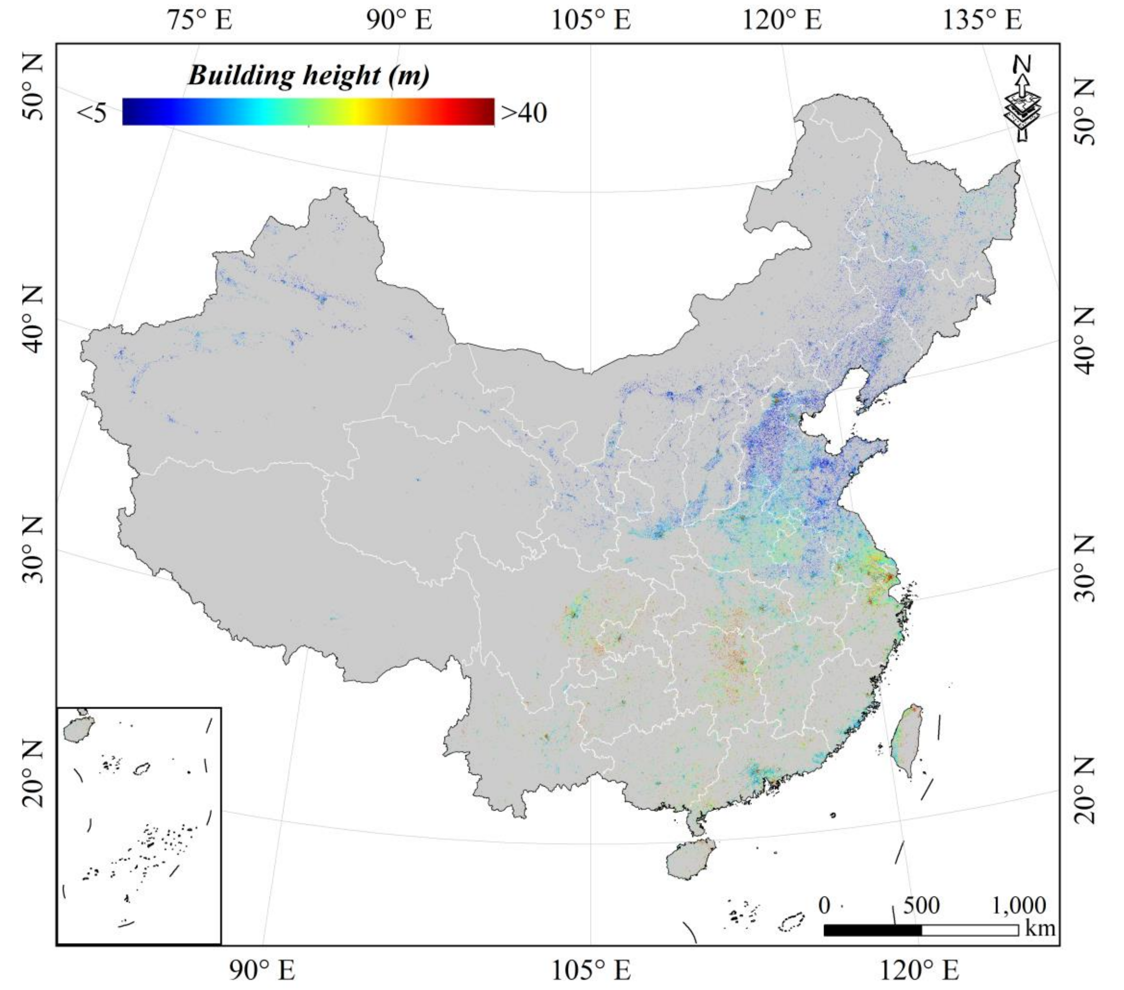

Fig. 8. Spatial distribution of building height in China (10 m spatial resolution), the dataset is freely available on Zenodo, and can be explored in the CNBH-10 m Explorer web app (https://wwanben1994.users.earthengine.app/view/cnbh10 mtest).

The CNBH-10m product demonstrably provides accurate representations of building heights in several urban areas, as illustrated in Figure 9. A comparison with high-resolution satellite imagery reveals that the product performs well in estimating point, linear, and clustered arrangements of high-rise buildings and accurately reflects low buildings in older urban areas, such as the historic city of Beijing.

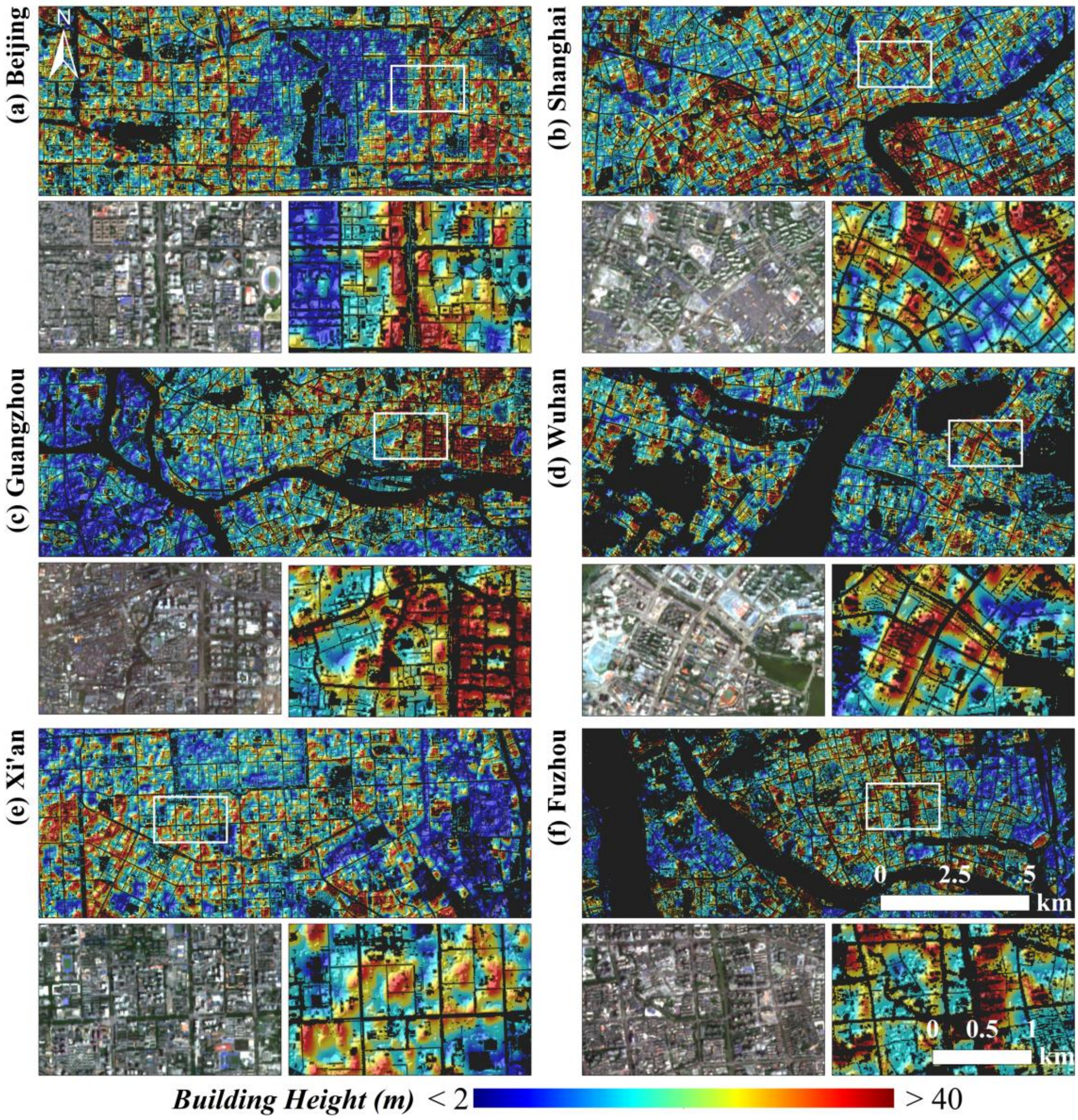

Fig. 9. Sub-samples (10 m spatial resolution) of building height from Beijing, Shanghai, Guangzhou, Wuhan, Xi’an and Fuzhou.

4.4 Regional distribution of building morphology

Based on the CNBH 10 m product, the mean building height at city level (Figure 10 a), the high-rise building area (Figure 10 b) and total building volume (Figure 10 c) are depicted for China. Macau (22.3 m) has the tallest, and Hong Kong (22.1 m) has the second tallest average building height. The larger metropolitan conurbations in China, i.e. Beijing, Shanghai, Guangzhou, and Shenzhen have mean building heights of 12.8 m, 18.0 m, 15.2 m, and 17.9 m, respectively. The distribution of the total area of high-rise buildings (above 24 m) in each city shows that the Beijing-Tianjin-Hebei region and the Yangtze River Delta region have more high-rise buildings, among which Shanghai has the most with 209.79 km^2, followed by Beijing (144.14 km^2), Suzhou (110.99 km^2) and Chongqing (106.29 km^2). There is a marked difference between the distribution of accumulated building volume and average building height at city scale. Cities with greater mean building heights are located especially along the coast and in central and southwestern China, while the largest building volumes are found in the most densely populated cities, such as Shanghai (298.4 10^8 m^3), Suzhou (266.8 10^8 m^3) and Beijing (266.2 10^8 m^3).

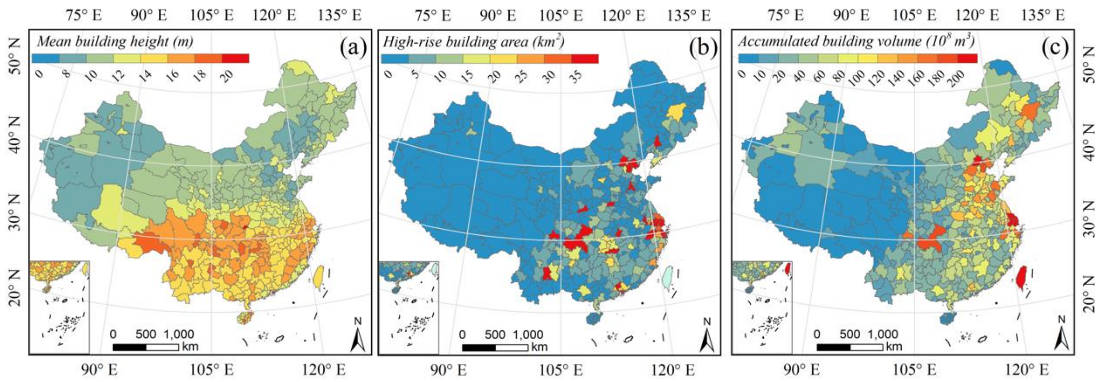

Fig.10. (a) Mean building height (b) High-rise building area (>24 m) and (c) Accumulated building volume at city level

4.5 The relationship between socio-economic parameters and building morphology

Using cities as a statistical unit, we compared population and GDP with building morphology, including mean building height, high-rise building area and accumulated building volume (Figure 11). The results show that building height generally does not correlate well with population or GDP, although high-rise building area and building volume exhibits a strong correlation with two socio-economic parameters. This may be due to the fact that most of the tall buildings are commercial sites and not located in residential areas. Population figure actually exhibits the most significant correlation with the high-rise building area (R^2=0.66, p-value<0.01) and building volume (R^2=0.78, p-value<0.01), while GDP also have very strong correlations with these two parameters.

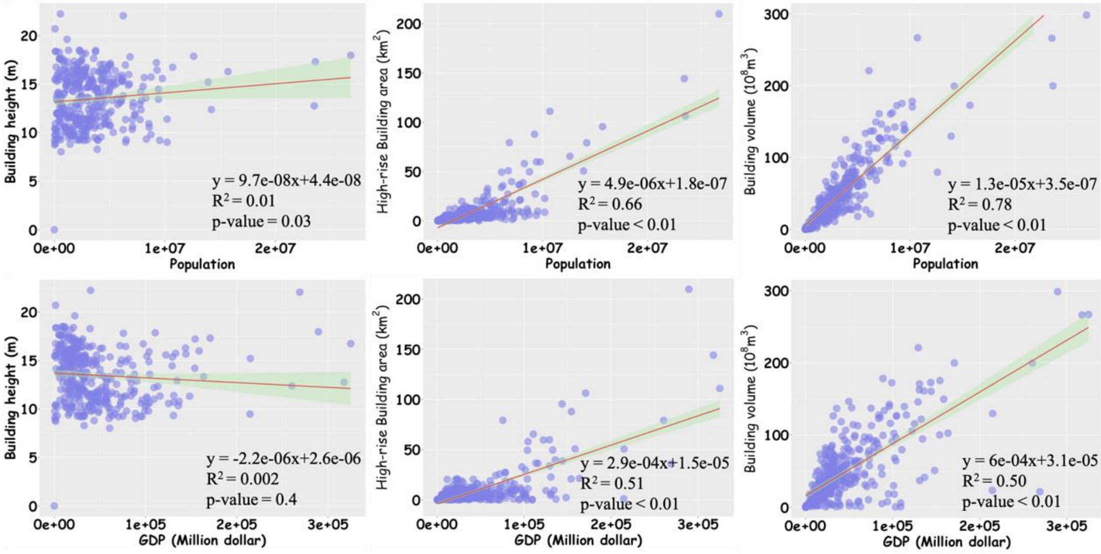

Fig. 11. Scatter plots of multiple socio-economic factors versus mean building height, high-rise building area and accumulated building volume at city scale. The total population, GDP was calculated in each city based on gridded population data (Sorichetta et al. 2015) and GDP product (Chen et al. 2022).

5. Discussion

5.1 The importance of independent variables on mapping building height

The backscattering coefficient is considered to have a strong correlation with building height, as demonstrated in previous studies (Li et al. 2020c; Yang and Zhao 2022). Accordingly, in this study we incorporate HH, HV polarization data from PALSAR to improve the accuracy of building height estimation. The complexity of urban morphology and urban building material differences introduces uncertainties if using only the backscatter coefficients for large scale and high resolution building height estimation. So in this study we also applied long time series optical data and explore application of the shading index. The results demonstrate that the backscatter coefficient and shading index are the most important variables in the building height estimation model.

In considering the large scale and complex topography of this national-scale study, information on building location and topography, as well as longitude, latitude, and

DEM were used to show that taking account of the relative contributions of these variables to the building height model can improve the generalizability of large-scale building height estimation. When estimating large scale building heights in China, which is more heterogeneous than those in European countries, the multi-window statistical approach used in this study effectively accounts for the model variables, such as shadows for high-rise and low-rise building. The study indicates that it is possible to improve the potential of building height estimation in such complex scenarios.

5.2 High accuracy of the building height map

In this study, we compared the estimated 10 m building height with existing sets of products, including 30 m (Huang et al. 2022), 500 m (Zhou et al. 2022), and 1000 m building heights (Li et al. 2020a). Figure 12 shows the distribution of building height observation data for six representative cities in China and compares the results across the four building heights. The results indicate that the 10 m building height product provides better detail and more accurately reflects the distribution pattern of building heights compared to other building height product. Furthermore, the 500 m and 1000 m building height products fail to reflect building height information at the block scale, thereby demonstrating the superiority of our 10 m building height product.

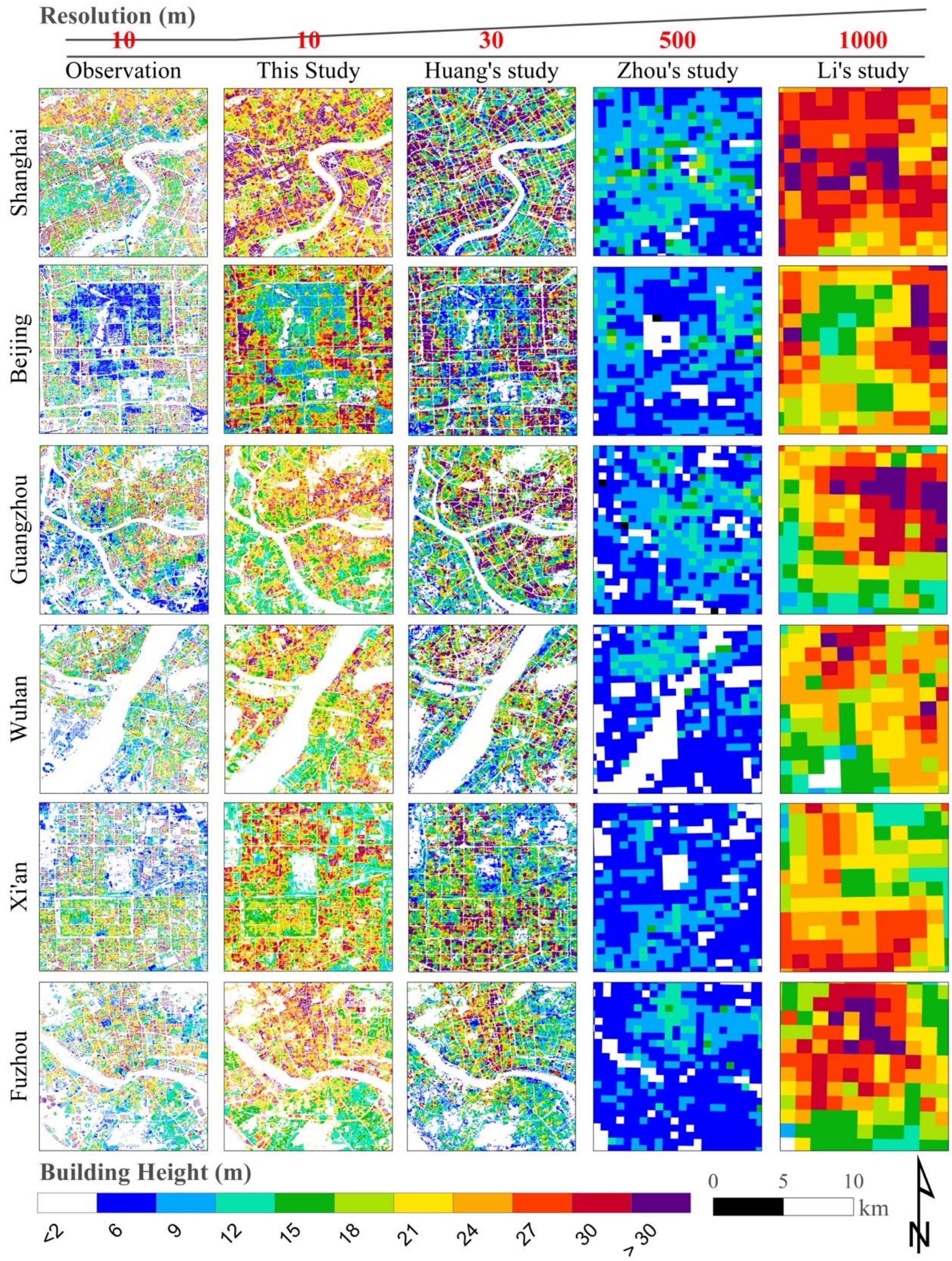

Fig. 12. Comparison of CNBH-10 m maps with multi-scale building height products for six Chinese cities

Additionally, we randomly selected 20,000 sample points and analyzed the correlation between the four sets of building height products (Figure 13). To ensure comparability of building height data across different resolutions, we resample the higher resolution data using the bilinear interpolation method to match the spatial resolution of the lower resolution data. Our findings show that the 10 m building height product has a good correlation with the 30 m and 1000 m building height products, with R values of 0.69 and 0.71, and RMSE values of 5.8 m and 4.4 m, respectively. However, the findings of this study exhibit a low correlation with the 500 m building height product, with an R value of only 0.41 and an RMSE value of 12.8 m. This may be due to the inclusion, in the 500 m building height product, of information on nonbuilding surfaces such as streets and parking lots (Zhou et al. 2022). This inclusion also explains the poor correlation between the 500 m and the 30 m and 1000 m building height products.

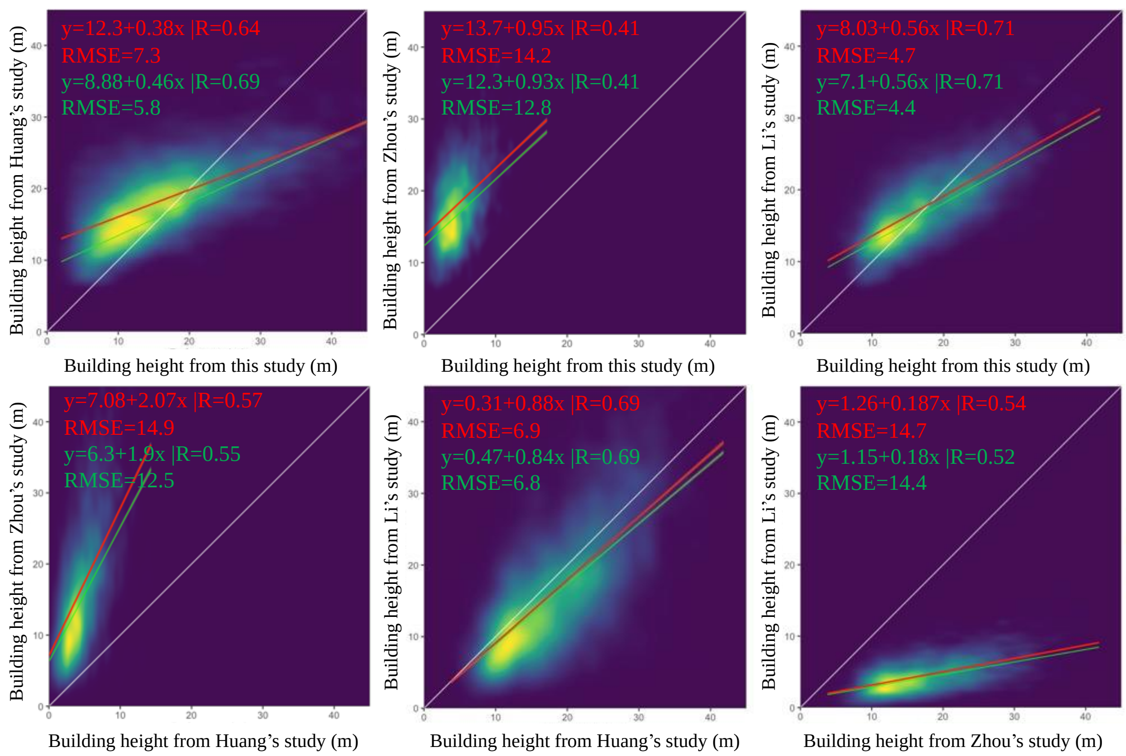

Fig. 13. Comparative analysis of multiple floor height products, white line: one-to-one, red line: ordinary least squares regression, green line: WLS regression, text in red: regression model, R value and RMSE of the ordinary least squares model, text in green: regression model, R value and RMSE of the WLS regression model.

5.3 Implications and uncertainties

Compared with the lower resolution building height products of previous studies (Li et al. 2020a; Li et al. 2020c; Yang and Zhao 2022), the 10 m spatial resolution building height data presented here demonstrates the feasibility of fine-grained urban 3D morphological characterization. Moreover, CNBH-10 m products provide potentially important baseline data with a wide range of applications, such as studies of urban microclimate. For example, previous researchers have indicated that the building complexity and the mixture of building types can influence urban ventilation and energy balance, and thus have effect on urban heat accumulation and release (Chun and Guldmann 2014). CNBH-10 m also has great potential in research on urban morphology. Specifically, there are numerous studies on the impact of urban expansion and urban 2D landscape patterns on urban ecology and the environment (Li et al. 2011; McDonald et al. 2020). However, the discontinuity and high economic cost of urban 3D data collection have made it difficult to quantify these impacts in cities. Together with the 3D building morphology metrics proposed in previous studies (Guo et al. 2021; Wu et al. 2017), CNBH10 m has great potential to fill this gap.

Despite these promising results, several limitations of the methodology need to be acknowledged. Due to the complex 3D structure and high degree of heterogeneity of cities, there are several uncertainties in the estimation of building height and these need to be carefully taken into account when applying the methodology. For example, additional shadows caused by trees and overpasses between buildings may affect the estimation of building height, future efforts to mitigate these uncertainties can be pursued through the utilization of multi-angle remote sensing techniques or the acquisition of higher-resolution satellite imagery (Kadhim and Mourshed 2017; Liu et al. 2020; Tripathy et al. 2022). The data resampling method used in the study may also have an impact on the results of the building height estimation. Here, the WSF dataset was used as the base map for building distribution, and a masking process was applied to the final CNBH-10m product. The accuracy of the base map has a significant influence on the accuracy of the building height product, especially for the building volume estimation. Future research could explore the combination of multiple building distribution products, such as GHS-BUILT-S2 (Corbane et al. 2021), to improve the accuracy. Due to the use of a pixel-based method for estimating building height, the final results of building height estimation exhibited some noise. Moreover, the multi-window approach used for processing input variables resulted in some smoothing effects in the building height products. To enhance the accuracy of building height estimation, future studies may consider utilizing object-based methods or employing post-processing techniques on building height products, in conjunction with more precise building boundaries such as vector boundaries of individual buildings (Milojevic-Dupont et al. 2023). The use of three-year remote sensing imagery for building height inversion in this study may also introduce uncertainties in the results due to rapid urban development in China. Moreover, due to computational limitations and mapping efficiency, this study only used the RF model for building height estimation and comparison, while further refinements may be achieved through deep learning methods. Although nighttime lighting and population data are also used as variables for building height estimation in the study, they do not contribute well to the building height estimation model, which is likely due to the low spatial resolution of these data..

6. Conclusion

This study demonstrates the potential of using earth observation data for national-scale building height estimation and establishes a high degree of accuracy of simulated building height based on RF regression modeling. Specifically, a total of 519 different feature variables were derived from earth observation data collected in all-weather conditions, and building heights were analyzed based on multitemporal, multispectral, and multiscale geospatial big data. The shading index, the backscattering coefficient, and the location of the building are the most significant contributors to the China-wide building height estimation model which has the potential for universality, transferability and reliability in terms of accuracy. Estimated and observed building heights exhibit R, RMSE and MAE values of 0.77, 6.1 m and 5.2 m respectively. In summary, the method and outputs indicate the potential of multi-source, multi-time, multi-window algorithms and cloud-based computing platforms for large-scale, refined building height mapping. The CNBH-10 m product can be applied to a wide range of urban process studies, such as urban climate, energy consumption and population estimates. The CNBH-10 m product is fully open source and freely available (https://zenodo.org/record/7064268#.YxtVAuxBz0p).

Declaration of Competing Interest

The authors declare that they have no known competing financial interests or personal relationships that could have appeared to influence the work reported in this paper.

Acknowledgements

This research was supported by the National Key Research and Development Project of China (grant no. 2021YFE0193100, 2018YFD0900806), European Union's Horizon 2020 research and innovation program (grant no. 821016) and China Scholarship Council (grant no. 202106100112).

Reference

Alahmadi, M., Atkinson, P., & Martin, D. (2013). Estimating the spatial distribution of the population of Riyadh, Saudi Arabia using remotely sensed built land cover and height data. *Computers, Environment and Urban Systems, 41*, 167-176

Borck, R. (2016). Will skyscrapers save the planet? Building height limits and urban greenhouse gas emissions. *Regional Science and Urban Economics, 58*, 13-25

Breiman, L. (2001). Random forests. *Machine learning, 45*, 5-32

Chen, J., Gao, M., Cheng, S., Hou, W., Song, M., Liu, X., & Liu, Y. (2022). Global 1 km× 1 km gridded revised real gross domestic product and electricity consumption during 1992–2019 based on calibrated nighttime light data. *Scientific Data, 9*, 1-14

Cheng, L., Zhang, F., Li, S., Mao, J., Xu, H., Ju, W., Liu, X., Wu, J., Min, K., & Zhang, X. (2020). Solar energy potential of urban buildings in 10 cities of China. *Energy, 196*, 117038

Chun, B., & Guldmann, J.-M. (2014). Spatial statistical analysis and simulation of the urban heat island in high-density central cities. *Landscape and Urban Planning, 125*, 76-88

Corbane, C., Syrris, V., Sabo, F., Politis, P., Melchiorri, M., Pesaresi, M., Soille, P., & Kemper, T. (2021). Convolutional neural networks for global human settlements mapping from Sentinel-2 satellite imagery. *Neural Computing and Applications, 33*, 6697-6720

Dai, K., Li, Z., Tomás, R., Liu, G., Yu, B., Wang, X., Cheng, H., Chen, J., & Stockamp, J. (2016). Monitoring activity at the Daguangbao mega-landslide (China) using Sentinel-1 TOPS time series interferometry. *Remote Sensing of Environment, 186*, 501-513

Drusch, M., Del Bello, U., Carlier, S., Colin, O., Fernandez, V., Gascon, F., Hoersch, B., Isola, C., Laberinti, P., & Martimort, P. (2012). Sentinel-2: ESA's optical high-resolution mission for GMES operational services. *Remote Sensing of Environment, 120*, 25-36

Frantz, D., Schug, F., Okujeni, A., Navacchi, C., Wagner, W., van der Linden, S., & Hostert, P. (2021). National-scale mapping of building height using Sentinel-1 and Sentinel-2 time series. *Remote Sensing of Environment, 252*, 112128

Ghosh, T., Coscieme, L., Anderson, S.J., & Sutton, P.C. (2020). Building volume per capita (BVPC): A spatially explicit measure of inequality relevant to the SDGs. *Frontiers in Sustainable Cities, 2*, 37

Gislason, P.O., Benediktsson, J.A., & Sveinsson, J.R. (2006). Random forests for land cover classification. *Pattern recognition letters, 27*, 294-300

Gong, P., Li, X., Wang, J., Bai, Y., Chen, B., Hu, T., Liu, X., Xu, B., Yang, J., & Zhang, W. (2020). Annual maps of global artificial impervious area (GAIA) between 1985 and 2018. *Remote Sensing of Environment, 236*, 111510

Gorelick, N., Hancher, M., Dixon, M., Ilyushchenko, S., Thau, D., & Moore, R. (2017). Google Earth Engine: Planetary-scale geospatial analysis for everyone. *Remote Sensing of Environment, 202*, 18-27

Guan, H., Li, J., Chapman, M., Deng, F., Ji, Z., & Yang, X. (2013). Integration of orthoimagery and lidar data for object-based urban thematic mapping using random forests. *International Journal of Remote Sensing, 34*, 5166-5186

Guo, F., Wu, Q., & Schlink, U. (2021). 3D building configuration as the driver of diurnal and nocturnal land surface temperatures: Application in Beijing's old city. *Building and Environment,* *206*, 108354

Huang, H., Chen, P., Xu, X., Liu, C., Wang, J., Liu, C., Clinton, N., & Gong, P. (2022). Estimating building height in China from ALOS AW3D30. *ISPRS Journal of Photogrammetry and Remote Sensing, 185*, 146-157

Huang, X., & Wang, Y. (2019). Investigating the effects of 3D urban morphology on the surface urban heat island effect in urban functional zones by using high-resolution remote sensing data: A case study of Wuhan, Central China. *ISPRS Journal of Photogrammetry and Remote Sensing, 152*, 119-131

Huete, A., Didan, K., Miura, T., Rodriguez, E.P., Gao, X., & Ferreira, L.G. (2002). Overview of the radiometric and biophysical performance of the MODIS vegetation indices. *Remote Sensing of Environment, 83*, 195-213

Kadhim, N., & Mourshed, M. (2017). A shadow-overlapping algorithm for estimating building heights from VHR satellite images. *IEEE Geoscience and Remote Sensing Letters, 15*, 8-12

Kedron, P., Zhao, Y., & Frazier, A.E. (2019). Three dimensional (3D) spatial metrics for objects. *Landscape ecology, 34*, 2123-2132

Koppel, K., Zalite, K., Voormansik, K., & Jagdhuber, T. (2017). Sensitivity of Sentinel-1 backscatter to characteristics of buildings. *International journal of remote sensing, 38*, 6298-6318

Lawrence, R.L., Wood, S.D., & Sheley, R.L. (2006). Mapping invasive plants using hyperspectral imagery and Breiman Cutler classifications (RandomForest). *Remote Sensing of Environment, 100*, 356-362

Li, J., Song, C., Cao, L., Zhu, F., Meng, X., & Wu, J. (2011). Impacts of landscape structure on surface urban heat islands: A case study of Shanghai, China. *Remote Sensing of Environment, 115*, 3249-3263

Li, M., Koks, E., Taubenböck, H., & van Vliet, J. (2020a). Continental-scale mapping and analysis of 3D building structure. *Remote Sensing of Environment, 245*, 111859

Li, X., Gong, P., Zhou, Y., Wang, J., Bai, Y., Chen, B., Hu, T., Xiao, Y., Xu, B., & Yang, J. (2020b). Mapping global urban boundaries from the global artificial impervious area (GAIA) data. *Environmental Research Letters, 15*, 094044

Li, X., Zhao, L., Li, D., & Xu, H. (2018). Mapping urban extent using Luojia 1-01 nighttime light imagery. *Sensors, 18*, 3665

Li, X., Zhou, Y., Gong, P., Seto, K.C., & Clinton, N. (2020c). Developing a method to estimate building height from Sentinel-1 data. *Remote Sensing of Environment, 240*, 111705

Liang, H., Guo, Z., Wu, J., & Chen, Z. (2020). GDP spatialization in Ningbo City based on NPP/VIIRS night-time light and auxiliary data using random forest regression. *Advances in Space Research, 65*, 481-493

Liaw, A., & Wiener, M. (2002). Classification and regression by randomForest. *R news, 2*, 18-22

Liu, C.-J., Krylov, V.A., Kane, P., Kavanagh, G., & Dahyot, R. (2020). IM2ELEVATION: Building height estimation from single-view aerial imagery. *remote sensing, 12*, 2719

Liu, M., Ma, J., Zhou, R., Li, C., Li, D., & Hu, Y. (2021). High-resolution mapping of mainland China's urban floor area. *Landscape and Urban Planning, 214*, 104187

Marconcini, M., Metz-Marconcini, A., Üreyen, S., Palacios-Lopez, D., Hanke, W., Bachofer, F., Zeidler, J., Esch, T., Gorelick, N., & Kakarla, A. (2020). Outlining where humans live, the World

Settlement Footprint 2015. *Scientific Data, 7*, 1-14

McDonald, R.I., Mansur, A.V., Ascensão, F., Crossman, K., Elmqvist, T., Gonzalez, A., Güneralp, B., Haase, D., Hamann, M., & Hillel, O. (2020). Research gaps in knowledge of the impact of urban growth on biodiversity. *Nature Sustainability, 3*, 16-24

Mertes, C.M., Schneider, A., Sulla-Menashe, D., Tatem, A., & Tan, B. (2015). Detecting change in urban areas at continental scales with MODIS data. *Remote Sensing of Environment, 158*, 331-347

Milojevic-Dupont, N., Wagner, F., Nachtigall, F., Hu, J., Brüser, G.B., Zumwald, M., Biljecki, F., Heeren, N., Kaack, L.H., & Pichler, P.-P. (2023). EUBUCCO v0. 1: European building stock characteristics in a common and open database for 200+ million individual buildings. *Scientific Data, 10*, 147

Ni, R., Tian, J., Li, X., Yin, D., Li, J., Gong, H., Zhang, J., Zhu, L., & Wu, D. (2021). An enhanced pixel-based phenological feature for accurate paddy rice mapping with Sentinel-2 imagery in Google Earth Engine. *ISPRS Journal of Photogrammetry and Remote Sensing, 178*, 282-296

Perini, K., & Magliocco, A. (2014). Effects of vegetation, urban density, building height, and atmospheric conditions on local temperatures and thermal comfort. *Urban Forestry & Urban Greening, 13*, 495-506

Pettorelli, N. (2013). *The normalized difference vegetation index*. Oxford University Press

Resch, E., Bohne, R.A., Kvamsdal, T., & Lohne, J. (2016). Impact of urban density and building height on energy use in cities. *Energy Procedia, 96*, 800-814

Rodriguez, E., Morris, C.S., & Belz, J.E. (2006). A global assessment of the SRTM performance. *Photogrammetric Engineering & Remote Sensing, 72*, 249-260

Schug, F., Frantz, D., van der Linden, S., & Hostert, P. (2021). Gridded population mapping for Germany based on building density, height and type from Earth Observation data using census disaggregation and bottom-up estimates. *Plos one, 16*, e0249044

Shimada, M., Itoh, T., Motooka, T., Watanabe, M., Shiraishi, T., Thapa, R., & Lucas, R. (2014). New global forest/non-forest maps from ALOS PALSAR data (2007–2010). *Remote Sensing of Environment, 155*, 13-31

Sorichetta, A., Hornby, G.M., Stevens, F.R., Gaughan, A.E., Linard, C., & Tatem, A.J. (2015). High-resolution gridded population datasets for Latin America and the Caribbean in 2010, 2015, and 2020. *Scientific Data, 2*, 1-12

Sun, G., Huang, H., Weng, Q., Zhang, A., Jia, X., Ren, J., Sun, L., & Chen, X. (2019). Combinational shadow index for building shadow extraction in urban areas from Sentinel-2A MSI imagery. *International Journal of Applied Earth Observation and Geoinformation, 78*, 53-65

Sun, X., Li, Q., & Yang, B. (2018). Compositional structure recognition of 3D building models through volumetric analysis. *IEEE access, 6*, 33953-33968

Torres, R., Snoeij, P., Geudtner, D., Bibby, D., Davidson, M., Attema, E., Potin, P., Rommen, B., Floury, N., & Brown, M. (2012). GMES Sentinel-1 mission. *Remote Sensing of Environment, 120*, 9-24

Tripathy, P., Balakrishnan, K., de Franchis, C., & Kumar, A. (2022). Generating megacity-scale building height maps without DGNSS surveyed GCPs: An open-source approach. *Environment and Planning B: Urban Analytics and City Science, 49*, 2312-2330

Tucker, C.J. (1979). Red and photographic infrared linear combinations for monitoring vegetation. *Remote Sensing of Environment, 8*, 127-150

Veci, L., Prats-Iraola, P., Scheiber, R., Collard, F., Fomferra, N., & Engdahl, M. (2014). The sentinel-

1 toolbox. In, *Proceedings of the IEEE International Geoscience and Remote Sensing Symposium (IGARSS)* (pp. 1-3): IEEE

Vreugdenhil, M., Wagner, W., Bauer-Marschallinger, B., Pfeil, I., Teubner, I., Rüdiger, C., & Strauss, P. (2018). Sensitivity of Sentinel-1 backscatter to vegetation dynamics: An Austrian case study. *Remote Sensing, 10*, 1396

Wang, N., Zhang, X., Yao, S., Wu, J., & Xia, H. (2022). How Good Are Global Layers for Mapping Rural Settlements? Evidence from China. *Land, 11*, 1308

Wu, Q., Guo, F., Li, H., & Kang, J. (2017). Measuring landscape pattern in three dimensional space. *Landscape and Urban Planning, 167*, 49-59

Wu, W.-B., Yu, Z.-W., Ma, J., & Zhao, B. (2022). Quantifying the influence of 2D and 3D urban morphology on the thermal environment across climatic zones. *Landscape and Urban Planning, 226*, 104499

Xi, C., Ren, C., Wang, J., Feng, Z., & Cao, S.-J. (2021). Impacts of urban-scale building height diversity on urban climates: A case study of Nanjing, China. *Energy and Buildings, 251*, 111350

Xiao, X., Hollinger, D., Aber, J., Goltz, M., Davidson, E.A., Zhang, Q., & Moore III, B. (2004). Satellite-based modeling of gross primary production in an evergreen needleleaf forest. *Remote Sensing of Environment, 89*, 519-534

Xu, H. (2006). Modification of normalised difference water index (NDWI) to enhance open water features in remotely sensed imagery. *International journal of remote sensing, 27*, 3025-3033

Yang, C., & Zhao, S. (2022). A building height dataset across China in 2017 estimated by the spatially-informed approach. *Scientific Data, 9*, 1-11

Zha, Y., Gao, J., & Ni, S. (2003). Use of normalized difference built-up index in automatically mapping urban areas from TM imagery. *International journal of remote sensing, 24*, 583-594

Zhang, Q., Schaaf, C., & Seto, K.C. (2013). The vegetation adjusted NTL urban index: A new approach to reduce saturation and increase variation in nighttime luminosity. *Remote Sensing of Environment, 129*, 32-41

Zhang, W., Li, W., Zhang, C., Hanink, D.M., Liu, Y., & Zhai, R. (2018). Analyzing horizontal and vertical urban expansions in three East Asian megacities with the SS-coMCRF model. *Landscape and Urban Planning, 177*, 114-127

Zhou, Y., Li, X., Chen, W., Meng, L., Wu, Q., Gong, P., & Seto, K.C. (2022). Satellite mapping of urban built-up heights reveals extreme infrastructure gaps and inequalities in the Global South. *Proceedings of the National Academy of Sciences, 119*, e2214813119

Zhu, Z., Zhou, Y., Seto, K.C., Stokes, E.C., Deng, C., Pickett, S.T., & Taubenböck, H. (2019). Understanding an urbanizing planet: Strategic directions for remote sensing. *Remote Sensing of Environment, 228*, 164-182